Robust and reliable actinic ptychographic imaging of highly periodic structures in EUV photomasks

Bin Wang, Nathan Brooks, Michael Tanksalvala, Yuka Esashi, Nicolas Jenkins, et al.

Bin Wang, Nathan Brooks, Michael Tanksalvala, Yuka Esashi, Nicolas Jenkins, Peter Johnsen, Iona Binnie, Guan Gui, YunZhe Shao, Margaret M. Murnane, Henry C. Kapteyn, "Robust and reliable actinic ptychographic imaging of highly periodic structures in EUV photomasks," Proc. SPIE 12293, Photomask Technology 2022, 122930D (1 December 2022); doi: 10.1117/12.2641726

SPIE.

Event: SPIE Photomask Technology + EUV Lithography, 2022, Monterey, California, United States

Robust and reliable actinic ptychographic imaging of highly periodic structures in EUV photomasks

Bin Wang*[a], Nathan Brooks[a], Michael Tanksalvala[a], Yuka Esashi[a], Nicolas Jenkins[a], Peter Johnsen[a], Iona Binnie[a], Guan Gui[a], YunZhe Shao[a], Margaret M. Murnane[a], Henry C. Kapteyn[a,b]
[a]STROBE Science and Technology Center, JILA and Department of Physics, University of Colorado, Boulder, CO, 80309, USA; [b]KMLabs Inc., 4775 Walnut St., Building 102, Boulder, CO, 80301, USA

ABSTRACT

As EUV lithography transitions to high volume manufacturing, actinic inspection tools at 13.5 nm wavelength are attractive for understanding the printability of EUV mask defects, as well as for in-fab monitoring for possible defects emerging from extended use. Coherent diffractive imaging (CDI) is a lensless imaging technique that allows for phase-and-amplitude, aberration-free, high-resolution imaging in the EUV. Moreover, sources based on high harmonic generation (HHG) of ultrafast lasers are a proven viable coherent light source for CDI, with flux sufficient for rapid large-area inspection and small-area imaging. By combining CDI and HHG, we implemented actinic EUV photomask inspection on a low-cost tabletop-scale setup. Moreover, we propose and demonstrate a solution to the challenge of ptychographic imaging of periodic structures through careful illumination engineering.

Keywords: extreme ultraviolet lithography, photomask, actinic, EUV, coherent diffractive imaging, high harmonic generation, metrology, periodic structures

1. INTRODUCTION

As extreme ultraviolet (EUV) lithography is moving to high volume manufacturing, the fabrication and inspection of defect-free EUV photomasks remains one of the most critical and challenging issues in EUV metrology [1-6]. Although some inspection can be done using DUV or electron beams, non-actinic inspection techniques struggle with low spatial resolution and/or exaggeration or distortion of the actual impact of photomask defects on patterned wafers. For example, it has been demonstrated that a photomask defect detected by electron beams can result in no impact on the patterned wafer [1], or vice versa. Consequently, an EUV actinic inspection tool is extremely attractive for inspection of the printability of EUV mask defects, as well as for in-fab monitoring for possible defects emerging from extended use.

However, current implementations of actinic review of masks using conventional reflective or zone-plate imaging are too expensive to be routinely employed. First, EUV microscopy using zone plate optics can inspect EUV masks with relatively high sensitivity and throughput [2]. But they can only provide amplitude images, i.e., no phase information, with resolution limited by the zone plate fidelity. Direct imaging with reflective optics is also possible, but with extreme demands on the optical figure and alignment [3]. In contrast, ptychography, as a particularly powerful approach to CDI, is a lensless imaging technique that allows phase-contrast, aberration-free and high-resolution imaging of semiconductor samples [7-10], including EUV photomasks. High-NA, diffraction-limited resolution can provide an unprecedented view of photomasks, making it possible to identify sub-threshold mask features that may evolve into printed defects. Furthermore, the phase information inherent in ptychographic images is very beneficial to numerical simulation tools for EUV technologies.

Ptychography has been used with synchrotron radiation to produce high quality images of EUV photomasks [4,6]—however, these sources have limited access. High harmonic generation [11-12] is a promising alternative to synchrotrons that can provide bright and coherent EUV light at 13.5nm. By combining HHG and ptychography, it is possible to implement actinic EUV mask inspection on a tabletop scale setup and at a reasonable cost. Although researchers have demonstrated ptychographic reconstruction of micron- and submicron-scale features, the quality and reliability of these images still needs validation, and the challenge of ptychographic imaging of highly periodic structures, for example, 1D line-space and 2D contact array structures, remains to be definitively addressed. This challenge is due to the lack of

*bin.wang-2@colorado.edu; phone +1(720) 285-8736

Photomask Technology 2022, edited by Bryan S. Kasprowicz, Proc. of SPIE Vol. 12293, 122930D · © 2022 SPIE · 0277-786X · doi: 10.1117/12.2641726

diversity in the diffraction data [5,9,13] used in ptychographic reconstruction. Consequently, a versatile tabletop-scale tool for robust and reliable actinic EUV photomask microscopy has not previously been implemented.

2. SYSTEM CONFIGURATION

STROBE, JILA, and KMLabs have jointly been developing a concept for a Tabletop-scale EUV Actinic Microscope System—TEAMS. The TEAMS configuration is detailed in this section. It contains two modules: (1) the EUV source and beamline, and (2) the ptychography microscope end-station. Optically, the goal is to deliver as much EUV flux at 13.5 nm wavelength from the source to a well-behaved illumination spot on the mask. Mechanically, a coarse translation stages is used to position the tool to specific locations on an EUV photomask, with a fine-scan nm-scale precision stage acting to obtain ptychographic data sets of micron-size regions of interest.

2.1 The EUV source

TEAMS is powered by a bright coherent tabletop HHG source at 13.5 nm wavelength driven by a Ti:sapphire laser. A Ti:sapphire driving laser (KMLabs RAEA^{TM}) operates at $\lambda \sim 790$nm with 30 fs pulse duration, 3 mJ pulse energy, and 5 kHz repetition rate (total output power 15 W). HHG up-conversion is done in a KMLabs XUUS$_4$, with the HHG occurring in a waveguide with ~ 1 atm helium gas target pressure. In this configuration, the HHG process is optimally phase matched, generating odd harmonics of the driving laser up to $h\nu \sim 120$ eV, with a flux of $\sim > 10^{10}$ ph/s/harmonic. A beamline separates the EUV beam from the driving laser, and a diagnostic beamline with a switchable mirror serves to optimize the spatial profile and flux of the EUV beam, as shown in Fig. 1(a). After the EUV beam is optimized, it is delivered to the lensless EUV microscope end-station, see Fig. 1(b).

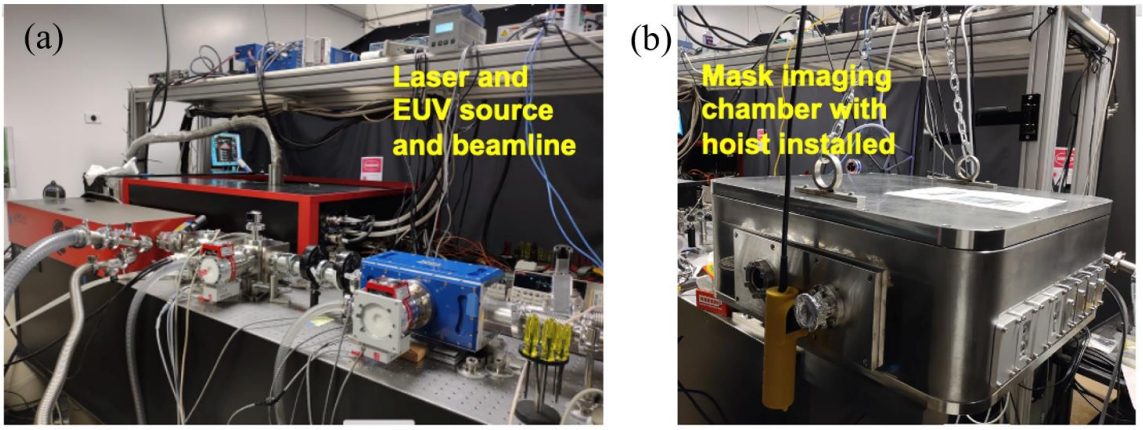

Figure 1. Photos show (a) the Ti:sapphire amplifier, XUUS for HHG, and diagnostic and beam delivery beamline, and (b) the actinic mask imaging end-station.

2.2 The lensless EUV microscope

The generated EUV HHG spectrum consists of a comb of the odd harmonic orders of the laser, of which the 57th or 59th correspond to the target illumination wavelength. Two Si/Mo multilayer mirrors are used to select $\lambda \sim 13.5$nm, with $\Delta\lambda/\lambda \sim 2\%$, for actinic ptychography imaging. The first mirror is a focusing mirror, M_S, with a 10cm radius of curvature at near-normal angle of incidence (AOI), while and the second mirror is a flat mirror, M_F, with 48 degrees AOI from normal. As shown in Fig. 2(a), the EUV illumination is incident from the left onto M_S, is focused. While the beam is focusing, M_F deflects the beam upward onto the EUV photomask at ~ 6 degrees from normal. Both mirrors are mounted on precision XYZ translation stage ensembles (SmarAct XYZ-SLC17:30) and can be precisely positioned in 3D space for alignment. Furthermore, M_F has an extra degree of freedom for rotation (SmarAct SRP20:13) to fine tune the angle of incidence onto M_F and the EUV photomask sample. The EUV photomask is mounted on a micro-scale precision XY translation stage ensemble (Griffin Motion XY stages) for coarse positioning over a large area (~100 x 100 mm^2). An EUV-CCD camera (Teledyne Princeton Instruments SOPHIA-XO 2048B-132, 2048 x 2048 imaging array, 13.5 x 13.5 um pixel size) is mounted below the sample, with the sensor facing up towards the sample and with a sample-to-sensor distance of ~ 40 mm, to capture the far-field diffraction patterns. A photo of the real apparatus can be found in Fig. 2(b).

The reflectivity vs wavelength curves for each individual mirror and for the combination of both mirrors can be found in Fig. 2 (c).

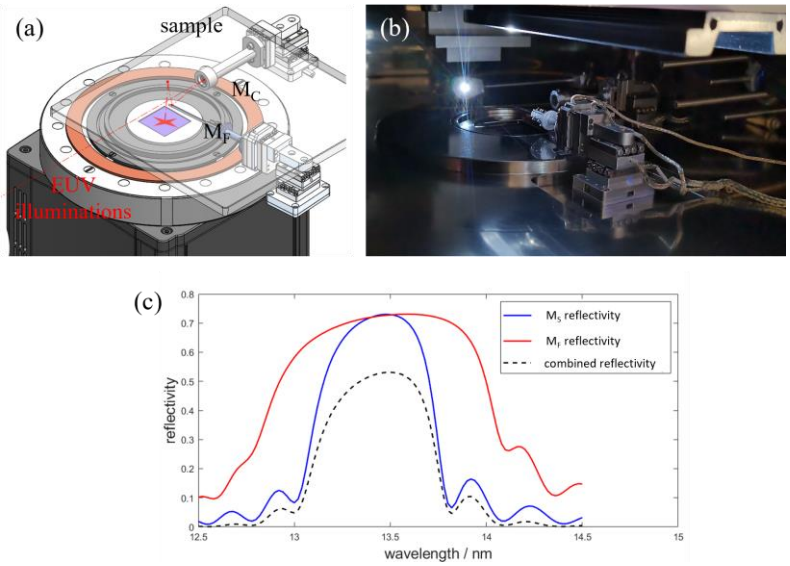

Figure 2. The lensless EUV microscope optical system in the imaging chamber consists of two Si/Mo multilayer mirrors, M_S and M_F, to select out a single wavelength at 13.5 nm wavelength and focus it onto the EUV photomask sample at a 6 degrees angle of incidence from normal. The EUV beam reflects and diffracts from the photomask and is collected by an EUV-CCD camera. (a) A schematic diagram and (b) a photo of the lensless EUV microscope. (c) The reflectivity vs wavelength curves for M_S, in blue, M_F, in red, and both mirrors, in dashed black.

2.3 Visible-light alignment microscope

Sample navigation is challenging for EUV imaging because the entire system must stay in high vacuum. We designed and installed an in-situ visible-light microscope with 10 um spatial resolution and a 2x2 mm^2 field of view to assist sample navigation in-situ. A white-light LED is coupled into the EUV microscope vacuum chamber through a fiber feedthrough to illuminate the sample—the bright light source in Fig. 2(b). Part of the reflected light from the sample is deflected by M_F into a single lens imaging system mounted on a cage system, and a CMOS camera is mounted on the outside-wall of the vacuum chamber to record images of the sample area. A reflective 1951 US Air Force test target, of which a photo is shown in Fig. 3(a), is used to align and test the alignment microscope. After it is aligned, a 2x2 mm^2 sample region in the red dashed box in Fig. 3(a) is imaged, resulting the image shown in Fig. 3(b).

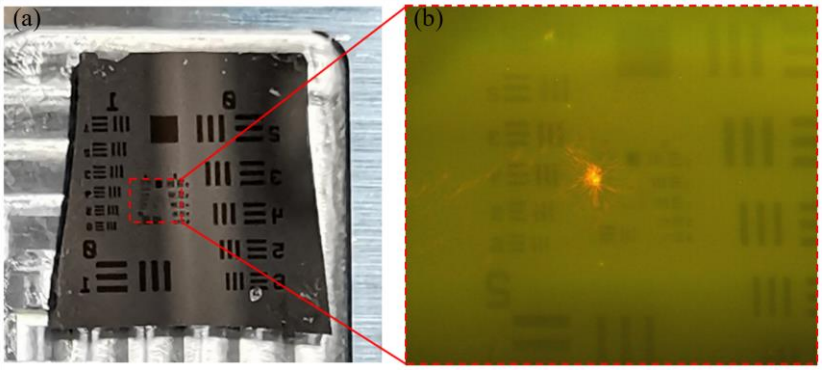

Figure 3. (a) This photo shows an USAF target for aligning the visible-light microscope. A 2x2 mm^2 region close to the center is imaged by the visible-light microscope, as shown in (b).

3. RESULTS

3.1 Visible laser demonstrations

The ptychography reconstruction algorithms are wavelength agnostic, providing diffraction-limited spatial resolution that scales directly with wavelength of the illumination. Likewise, the CCD works well for both visible and EUV detection. Thus, we validated operation of the system and verified its performance by demonstrating ptychographic imaging on two test samples using visible laser illumination, see Fig. 4(a).

Firstly, using a He-Ne laser at 632nm wavelength, we imaged a 1951 USAF test target. Figure 4(b) shows the amplitude of a ptychographic reconstruction of a 1951 USAF test target. The smallest features in this field of view, i.e., the horizontal and vertical bars from element 6 in group 5 with 8.77um linewidth, are clearly resolved with excellent fidelity, corresponding to a spatial resolution of at least 17.54um, while the diffraction-limited resolution is calculated to be 7.31um.

Secondly, we used a diode laser at slightly shorter wavelength, 405nm, to image a semiconductor sample from imec [12]. This sample is more challenging for two reasons: (1) The sample has low contrast, which leads to low diffraction efficiency into high orders and low SNR; (2) The sample is covered with 2D periodic arrays (a 3.6um pitch) of square pillars (1.8um lateral size), which is challenging for ptychography due to the lack of diversity in diffraction patterns [5,9,13]. The amplitude image of a ptychographic reconstruction is shown in Fig. 4(c), where the large features, such as the letters and the squares, are clearly resolved while the 2D periodic arrays still need improvement. This can be accomplished by better system calibration and alignment, using other test samples with higher contrast (either in amplitude or phase), and detector cooling or high dynamic range for higher SNR.

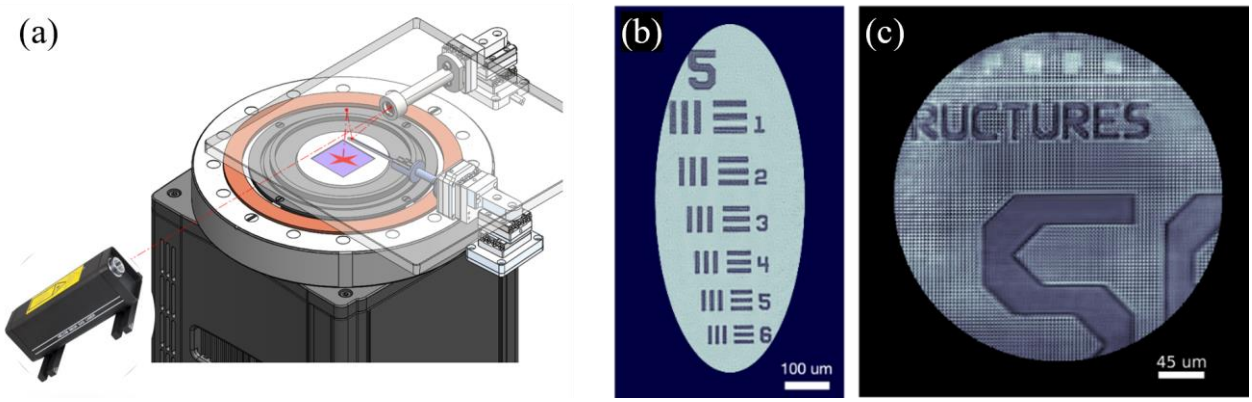

Figure 4. (a) A schematic shows the coupling of a visible laser to the lensless imaging end-station for troubleshooting and preliminary demonstrations. (b) The amplitude of a ptychographic reconstruction of a 1951 USAF test target taken with a He-Ne laser at 632nm wavelength, showing excellent image quality and a spatial resolution of at least 17.54um (element 6 in group 5), while the diffraction-limited spatial resolution is 7.31um. (c) the amplitude of a ptychographic reconstruction of a semiconductor test sample from imec taken with a diode laser at 450nm wavelength.

3.2 First EUV actinic imaging results

We successfully used TEAMS to image the nanoscale line-space (L/S) structures in an EUV photomask provided by imec, as shown in Fig. 1 and 2. The full EUV HHG beamline starts with the $XUUS_4$ to generate the illumination. The EUV is separated from the infrared driving laser first by reflecting from two rejector mirrors that transmit the driving laser and reflect the EUV beam, and then using 800nm-thick Zr filters to further filter out lower-order harmonics with a ~6% transmission at 13.5nm wavelength. An in-vacuum adjustable iris ~3 meters after the source is used to define the EUV mode. After it enters the end-station, the EUV beam reflects off the two Si/Mo multilayer mirrors, M_S and M_F, which selects out a single wavelength at 13.5nm with a combined reflectivity of ~50%. The total flux at 13.5nm incident onto the EUV photomask was estimated to be about $2.3x10^8$ photons per second. A 16-bit EUV-CCD camera is installed approximately 40mm away from the EUV photomask, which is equivalent to a numerical aperture (NA) of 0.3456 and a pixel size of 20nm in the reconstructed image. The EUV-CCD camera was cooled to -20℃ under ultra-high vacuum to reduce the noise level. The sample is an EUV photomask from imec that is designed to perform defectivity testing on 27nm L/S patterns—27nm half-period on the wafer corresponding to 216 nm full period on the mask itself. The ptychography scans were carried out by laterally scanning the spherical Si/Mo multilayer mirror, M_S, causing the beam

focus to move along with the mirror without changing the beam profile. We acquired a ptychography scan at 100 scan positions arranged in a 10 x 10 rectangular grid, with average nearest-neighbor spacing of 200nm and random offset at each position of up to 40nm to avoid gridding artifacts. The CCD integration time is set to 10 second, which nearly saturates the CCD. The far-field diffraction patterns consist of several completely separated diffraction orders, and the diffraction efficiencies slightly change as one scans the beam relative to the periodic L/S pattern. The complex images of the sample and the beam are reconstructed simultaneously using the ePIE algorithm [7]. The reconstructed beam in the sample plane is shown in Fig. 5(a), with a $1/e^2$ diameter of ~ 1um. A lineout of the beam intensity along the white dashed line in Fig. 5(a) is shown in Fig. 5(b). In the reconstruction process, we also applied total variation (TV) regularization to improve reconstruction fidelity. More specifically, every 5 reconstruction iterations, we used an open access TV regularization package [14] with a regularization parameter of 0.005 on the real and imaginary parts of the sample image in the high-fidelity region, and used as the object guess for the next iteration the mean of the regularized and original images. The TV regularization greatly suppressed the noise in the reconstruction and made the grating lines very sharp, as shown in Fig. 5(c) and 5(d) for the amplitude and phase, respectively. Moreover, we averaged the amplitude and phase of the reconstructed L/S pattern along the line direction, and plotted the lineouts in Fig. 5(e) and 5(f).

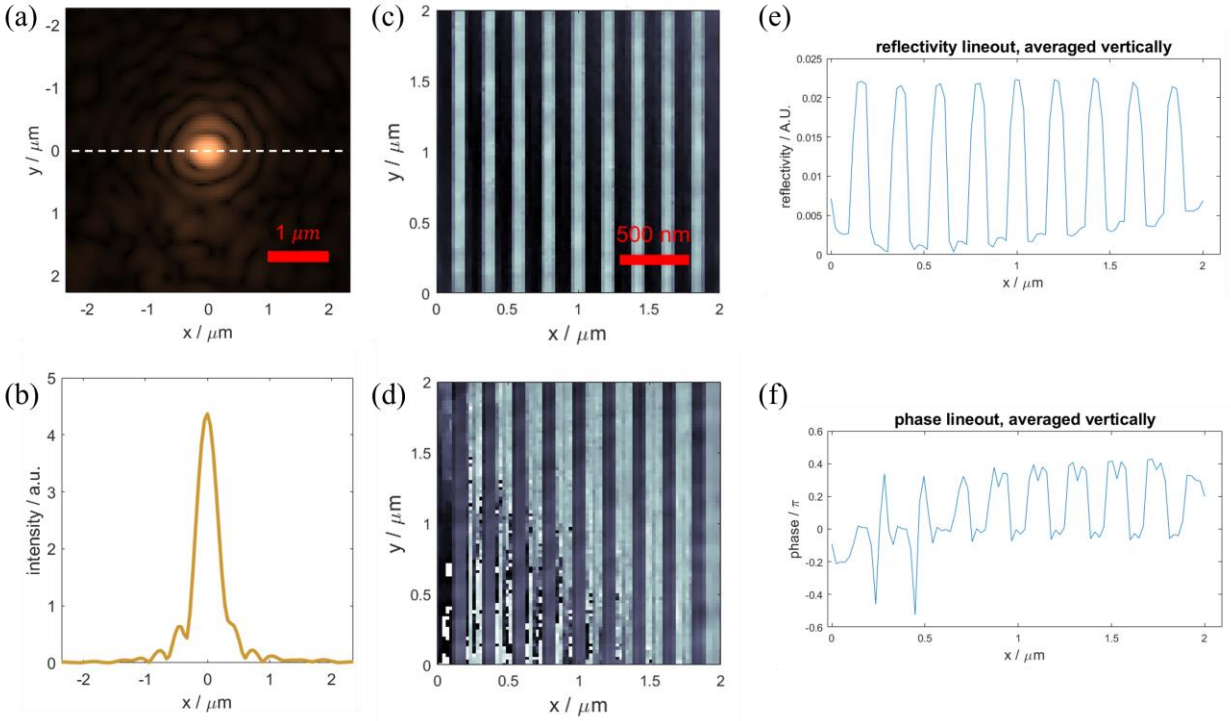

Figure 5. (a) The reconstructed beam intensity at 13.5nm wavelength. A lineout along the white dashed line is shown in (b). (c-d) The reconstructed amplitude and phase images of the 27nm L/S patterns on the EUV photomask. (e-f) The averaged cross-section of the 27nm L/S patterns.

3.3 Robust and reliable ptychographic imaging of highly periodic structures using a high harmonic EUV source

Robust and reliable imaging of highly periodic structures remains one of the most challenging problems for ptychography, as seen both in previous publications [5,9,13] and in the results shown above. Special treatments must be applied during the reconstruction process to improve the image quality, for example, modulus enforced probe was used by Gardner et al. in [9] and by Kim et al. in [13], and TV regularization was necessary to realize the results shown above. Ptychography relies on diversity in the diffraction patterns as one scans the beam relative to the sample making it possible to uniquely and robustly reconstruct the sample images. However, this diversity can be missing in the case of diffraction from highly periodic structures—the diffraction data can simply consist of isolated diffraction peaks from a grating—which makes them challenging to image via ptychography. To remedy this, we need to create diversity in the ptychography datasets. In a separate series of experiments using a simpler setup, we illustrated how to accomplish this, demonstrating robust and reliable ptychographic imaging of 2D highly periodic structures by designing the illuminating

beam such that the diffraction orders in the far-field overlap and interfere with each other. These interference fringes change in shape and position as one scans the beam relative to the sample, creating a large amount of data diversity that enables the robust and reliable ptychographic reconstructions of periodic structures.

In this experiment, we used coherent EUV light at 56nm wavelength, corresponding to the 7th harmonic of 390 nm. This wavelength can easily be isolated from lower and higher harmonic orders using thin metal filters. The EUV beam is then consecutively focused by two toroidal mirrors in a Wolter configuration that creates a focusing system with short effective focal length of 17cm (higher focusing NA) while managing coma aberration [15]. The test sample is a Quantifoil holey carbon film (9um pitch, 7um square holes and 2um thin carbon bars) mounted on a standard Ted Pella Ø3mm 200 mesh Cu TEM grid (125um pitch, 90um holes and 35um bars). An in-vacuum iris was installed before the focusing system to allow direct control of the divergence of the HHG illumination. We set the in-vacuum iris at four different aperture sizes, and for each case took a ptychography dataset at 49 scan positions arranged in a 7 x 7 rectangular grid, with average nearest-neighbor spacing of 3.33um and random offset at each position of up to 0.66um to avoid gridding artifacts. At each scan position, diffraction patterns were acquired with two exposure times—0.2 and 2 seconds—with data combined to for higher dynamic range. The beam diameter in the sample plane is about 20um. The ptychographic scan grids were set up such that the EUV beam only sees the carbon film mesh but does not see the Cu TEM grid, thus the field of view is highly periodic.

With the in-vacuum illumination definition iris set small to generate a relatively collimated illumination such that diffraction orders in the far-field do not overlap, as shown in Fig. 6(a-b), the reconstructions were dominated by gridding artifacts and failed, as shown in Fig. 6(e-f). However, when we further open the iris such that diffraction orders overlap with each other, interference patterns were observed in the overlapped area, as shown in Fig. 6(c-d). With the basic ePIE algorithm and minimal amount of effort, both datasets were reconstructed with high image quality and reliability, which strongly supports the validity of our technique, also providing a clear experimental criterion for reliable reconstruction of near-periodic structures.

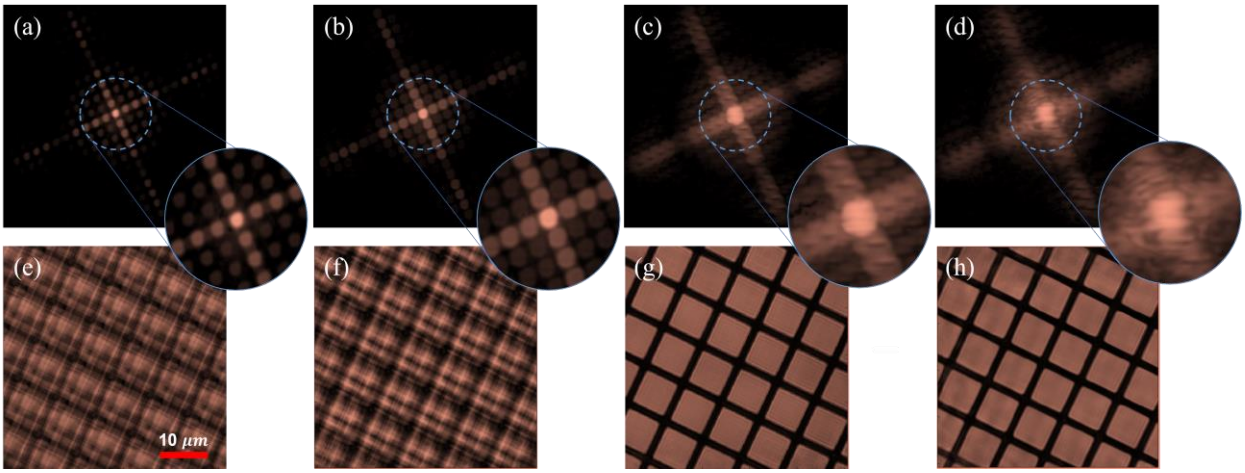

Figure 6. Example diffraction intensity patterns (a-d) and reconstructed amplitude images (e-h) under four experimental conditions in which the source divergence angles are controlled by an in-vacuum adjustable iris from small, i.e., no overlap in diffraction orders, to large, i.e., sufficient overlap in diffraction orders. A scale bar is shown in (e) and are shared among (e-h).

3.4 OAM HHG illuminations enable better ptychographic imaging of periodic structures

Recently, by incorporating the conservation of orbital angular momentum (OAM) of light [16-18], into the HHG process, researchers have gained unprecedented control over the properties of EUV light sources, including the divergence angle. HHG beams naturally have a significantly increased divergence (i.e., illumination NA) compared to that of Gaussian HHG beams. This optically enhanced NA allows us to achieve area overlap among diffraction orders for smaller pitch periodic samples beyond what is possible with the Gaussian probe, without making any changes to the focusing optics. Furthermore, the donut-shaped intensity distribution of OAM HHG beams ensures that the majority of photons fall in the overlap area (in contrast to the Gaussian beam, for which the overlap between diffraction orders

occurs at the tails of the intensity distributions), which increases the SNR for the interference fringes. Here, we demonstrate that these intrinsic advantages of OAM HHG beams enable better ptychographic imaging of highly periodic structures than traditional Gaussian HHG beams.

For generating HHG beams carrying OAM, we inserted a spiral phase plate (Holo-Or) to generate a driving beam with OAM charge number ℓ = 1, and λ = 395 nm. Due to the conservation of OAM in HHG, the resulting quasi-monochromatic 7th harmonic beam (λ = 56 nm) carries an OAM charge number of ℓ = 7, which has about three times divergence angle of corresponding Gaussian beams. The rest of the experimental setup remains the same.

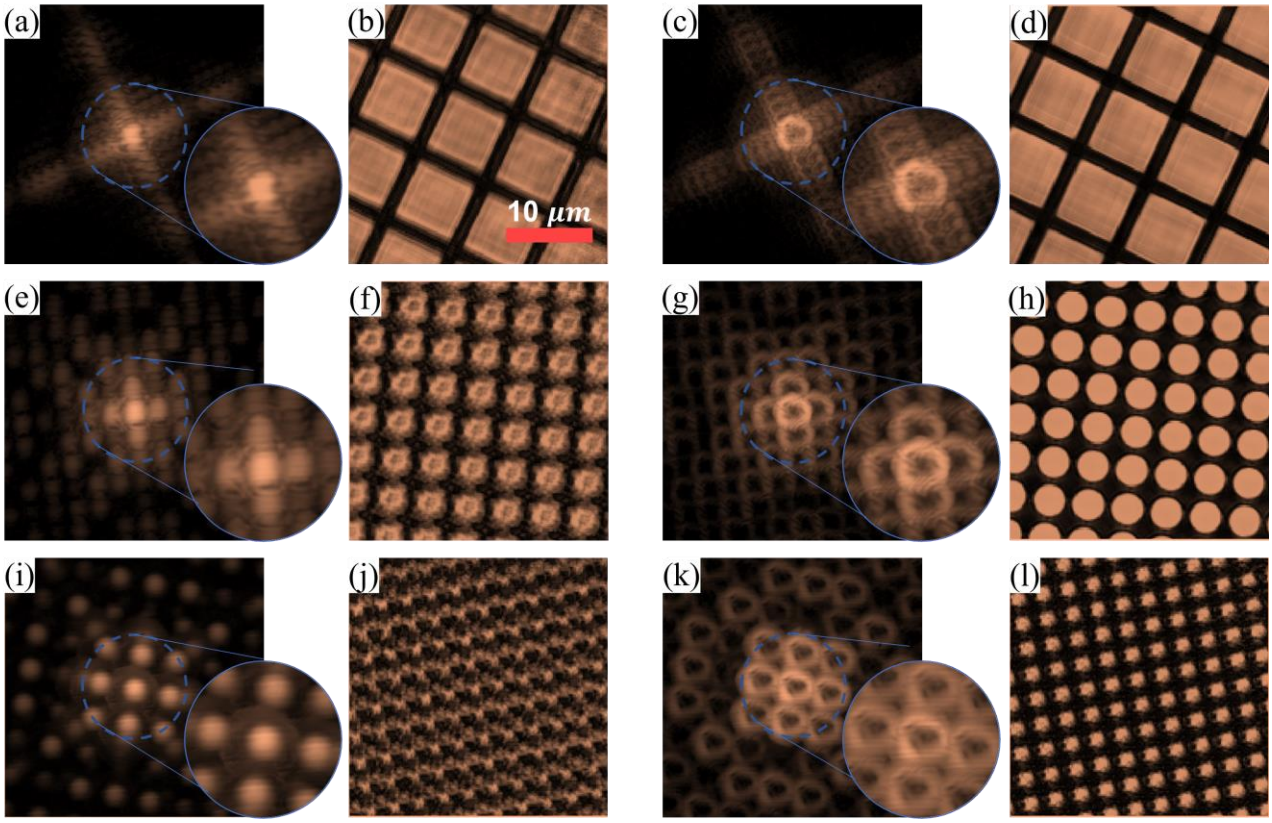

Figure 7. Comparison of ptychographic imaging quality between Gaussian HHG and OAM HHG illuminations. For a periodic structure with 9um pitch, example diffraction intensity patterns (a,c) and reconstructed amplitude images (b,d) are shown for Gaussian HHG and OAM HHG illuminations, respectively. The insets in (a) and (c) show interference fringes among multiple diffraction orders, and both cases result in high-quality reconstructions. For a periodic structure with 4.5um pitch, diffraction orders have larger separation. Example diffraction intensity patterns (e,g) and reconstructed amplitude images (f,h) are shown for Gaussian HHG and OAM HHG illuminations, respectively. The inset in (e) shows a small amount of interference for Gaussian HHG illuminations and the quality in (f) is degraded, while OAM HHG illuminations still result in significant interference, as shown in the inset in (g), thus high-quality reconstructions. For a periodic structure with 3um pitch, diffraction orders have even larger separation. Example diffraction intensity patterns (i,k) and reconstructed amplitude images (j,l) are shown for Gaussian HHG and OAM HHG illuminations, respectively. The inset in (i) shows no interference for Gaussian HHG illuminations and the reconstruction failed, as shown in (f), while OAM HHG illuminations still maintain a small amount of interference, as shown in the inset in (k), thus resulting in successful but low-quality reconstructions.

The testing samples are three Quantifoil holey carbon films which have various hole sizes and shapes arranged in a rectangular grid, and are mounted on standard Ted Pella Ø3mm Cu TEM grids with 200 mesh (125 um pitch, 90 um hole

width and 35 um bar width). More specifically, the three Quantifoil holey carbon films have pitches of 9 um (7 um square hole and 2 um bar, product number 656-200-CU), 4.5 um (3.5 um diameter circular holes and 1 um separation, product number 660-200-CU) and 3 um (2 um diameter circular holes and 1 um separation, product number 661-200-CU), respectively. For the 9 um pitch sample, both Gaussian and OAM HHG illuminations can produce a decent amount of interference, as shown in Fig. 7(a) and 7(c), which enables successful ptychographic reconstructions, as shown in Fig 7(b) and 7(d). OAM HHG illuminations produce higher quality reconstructions than Gaussian HHG due to the intrinsic larger divergence angle and donut-shaped intensity distribution. For the 4.5 um pitch sample, the separation among diffraction orders gets larger. The diffraction interference for Gaussian HHG illuminations is great decreased, in Fig. 7(e), which results in poor reconstruction quality in Fig. 7(f), while OAM HHG illuminations managed to maintain enough interference to yield high-fidelity reconstructions, Fig. 7(g-h). For the 3 um pitch sample, diffraction orders are even further separated. It causes the complete separation among diffraction orders and failure in ptychographic reconstructions for Gaussian HHG illuminations. However, OAM HHG beams still managed to image the periodic structure, even though the quality of the unit cell is poor. All datasets have a similar total number of photons.

4. FUTURE WORK

The goal of TEAMS is to perform high-fidelity inspection and imaging of EUV photomasks at high enough speed that meets the industry standards. We are currently working to refine the system by: (1) designing and installing a new EUV focusing system to deliver a focused beam with a higher illumination NA, which will improve the imaging fidelity and reliability; and (2) improving imaging throughput by taking advantage of state-of-the-art EUV CMOS cameras, which have a readout frame rate of about 20 frames per second as opposed to 0.5 frames per second for EUV CCD cameras. Improvements in efficiency of the EUV beamline, for example, by reducing the Zr filter thickness from 800nm to 200nm can increase the beamline efficiency by an order of magnitude and allow us to take advantage of these higher frame rates.

5. SUMMARY

In summary, we successfully implemented a tabletop EUV actinic microscope system (TEAMS) combining HHG and ptychography. We accomplished system calibrations and proof-of-concept demonstrations of ptychographic imaging capability by first using visible lasers to image some test samples and then using an HHG source at 13.5nm to image L/S patterns in an EUV photomask. We have separately validated a solution to challenges in ptychographic imaging of periodic structures Several future upgrades of the system are planned to achieve fast, reliable and high-fidelity inspection and imaging of EUV photomasks.

6. ACKNOWLEDGEMENTS

The authors wish to acknowledge Dr. John Peterson at imec for fruitful discussions and for providing us with the EUV photomask sample. This work was funded by DARPA STTR (grant# 140D0419C0094) and the NSF STROBE STC (DMR-1548924).

REFERENCES

[1] I. Mochi, K. A. Goldberg, B. La Fontaine, A. Tchikoulaeva, and C. Holfeld, *Proc. SPIE Extreme Ultraviolet (EUV) Lithography* **7636**, 76361A (2010).
[2] H. Miyai, T. Kohyama, T. Suzuki, K. Takehisa, and H. Kusunose, *Proc. SPIE Photomask Technology* **11148**, 111480W (2019).
[3] R. Capelli, M. Dietzel, D. Hellweg, M. Koch, G. Kersteen, K. Gwosch, D. Pagel, *Proc. SPIE Extreme Ultraviolet (EUV) Lithography* **10957**, 109570X (2019).
[4] I. Mochi, S. Fernandez, R. Nebling, U. Locans, P. Helfenstein, R. Rajeev, A. Dejkameh, D. Kazazis, L.-T. Tseng, and Y. Ekinci, *Proc. SPIE Extreme Ultraviolet (EUV) Lithography* **10957**, 109570W (2019).
[5] Y. Nagata, T. Harada, T. Watanabe, H. Kinoshita, and K. Midorikawa, *Int. J. Extrem. Manuf.* **1,** 032001 (2019).
[6] I. Mochi, H.-S. Kim, U. Locans, A. Dejkameh, R. Nebling, D. Kazazis, and Y. Ekinci, *Proc. SPIE Extreme Ultraviolet (EUV) Lithography* **11323**, 113231I (2020).
[7] A. M. Maiden, J. M. Rodenburg, Ultramicroscopy 109, 10 (2009).

[8] D. F. Gardner, M. Tanksalvala, E. R. Shanblatt, M. M. Murnane, H. C. Kapteyn, and D. E. Adams, Optica 1, 1 (2014).
[9] D. F. Gardner, et. al., Nat. Photon. 11, 259-263 (2017).
[10] M. Tanksalvala, et. al., Sci. Adv. 7, 5 (2021).
[11] A. Rundquist, C. G. Durfee III, Z. Chang, C. Herne, S. Backus, M. M. Murnane, and H. C. Kapteyn, *Science* **280,** 5368 (1998).
[12] R. A. Bartels, A. Paul, H. Green, H. C. Kapteyn, M. M. Murnane, S. Backus, I. P. Christov, Y. Liu, D. Attwood, and C. Jacobsen, *Science* **297**, 5580 (2002).
[13] Y. W. Kim, *et. al.*, *Appl. Phys. Express* **15**, 076505 (2022).
[14] A. Beck, M. Teboulle, *IEEE Trans. Image Process.* **18**, 2419-2434 (2009).
[15] H. Coudert-Alteirac, *et al.*, *Appl. Sci.* **7**, 1159 (2017).
[16] C. Hernández García, *et al.*, *Phys. Rev. Lett.* **111**, 083602 (2013).
[17] G. Gariepy, *et. al.*, *Phys. Rev. Lett.* **113**, 153901 (2014).
[18] R. Géneaux, *et. al.*, *Nat. Commun.* **7**, 12583 (2016).